Character of the Cd distribution in ultrathin CdSe layers in a ZnSe matrix

D. Litvinov, A. Rosenauer, and D. Gerthsen
Laboratorium für Elektronenmikroskopie, Universität Karlsruhe (TH), Kaiserstrasse 12, 76128 Karlsruhe, Germany

N. N. Ledentsov
Institut für Festörperphysik, Technische Universität Berlin, Hardenbergstrasse 36, 10623, Berlin, Germany
(Received 20 July 1999; revised manuscript received 27 January 2000)

The character of Cd distribution and the morphology of CdSe layers with nominal thicknesses between 0.7 and 3.6 ML in a ZnSe matrix were studied by conventional transmission electron microscopy (TEM) and high-resolution transmission electron microscopy (HRTEM) using plan-view and cross-section TEM samples. The Cd distribution was determined on an atomic scale by two different techniques. The first method is based on the measurement of local lattice parameters from zone-axis HRTEM images. The second technique relies on the evaluation of Fourier amplitudes derived from off-axis lattice fringe images. Continuous $Cd_xZn_{1-x}Se$ layers are observed, which are significantly broadened compared to the nominal thicknesses. The layers contain Cd-rich inclusions (small islands) with a size of less than 10 nm, and regions with a lower Cd concentration. With increasing nominal CdSe thickness, the Cd concentration and the island density increase. In addition, larger islands with a density two orders of magnitude below the small island density and a shape asymmetry are found in the 3.6-ML CdSe layer. The results are discussed with respect to the impact of the averaging effect caused by the finite TEM foil thickness on the measured Cd content in the Cd-rich islands and the surrounding region.

I. INTRODUCTION

Heterostructures containing CdSe with a nominal thickness of a few monolayers embedded in a ZnSe matrix have recently been the subject of increasing interest, motivated by the prospect of obtaining CdSe quantum-dot structures for fundamental studies and device applications. Due to the large lattice-parameter mismatch of 7.2%, the CdSe growth on ZnSe is expected to occur in the Stranski-Krastanow mode, comparable to the growth of InAs on GaAs, where three-dimensional (3D) islands nucleate on 2D wetting layer.[1,2] The generation of islands is energetically favorable compared to a two-dimensional, tetragonally strained layer, because the islands are able to elastically relax the lattice mismatch at their free surfaces. Reflection high-energy electron-diffraction RHEED patterns indeed revealed the transition from a two- to a three-dimensional growth mode at a CdSe thickness close to the critical one (about 3 ML) during the molecular-beam-epitaxy (MBE) growth.[3,4]

Several transmission electron microscopy (TEM) and atomic force microscopy (AFM) studies were already published, which are concerned with the structural properties of the CdSe deposits. AFM investigations of uncapped CdSe layers[5–11] revealed the presence of islands which are typically larger than 20 nm. However, there are strong indications that the results are not representative of buried layers, because a ripening of the islands was observed depending on the time after the removal from the growth chamber. In addition, the chemical nature of these islands was not completely clarified, because they were also observed on ZnSe with a submonolayer CdSe deposition[11] and even without CdSe at all.[6,12] Therefore, a distinction must be made between results obtained by AFM from uncapped island structures and those from capped CdSe layers studied by TEM.

The TEM results for ZnSe-capped structures differ considerably depending on the nominal thickness of the CdSe layer and the growth technique. Leonardi *et al.*[13] observed the transition from a continuous, two-dimensional layer into a layer with distinct thickness fluctuations in conventional cross-section TEM images, which can be correlated with the corresponding change of the RHEED pattern. Comparable results were obtained by Hommel *et al.*,[6] who observed a critical wetting layer thickness between 3.5 and 5 ML for the 2D/3D transition. At a CdSe thickness of 3 ML, Kirmse *et al.*[14] found a bimodal island distribution. The plan-view TEM strain contrast indicates the presence of small islands with sizes of less than 10 nm and an area density of about 10^{10} cm^{-2}, as well as larger islands with extensions between 10 and 50 nm with a density of 2×10^{9} cm^{-2}. More detailed studies of the continuous CdSe layers with nominal thicknesses below 3 ML by cross-section high resolution TEM (HRTEM) revealed a laterally inhomogeneous Cd distribution with Cd-rich inclusions of approximately 5-nm size.[14–18]

Of particular interest are the layers with $t_n<3$ ML, which show the signatures of the three-dimensional exciton confinement in the optical spectra, although a change of the RHEED pattern corresponding to the three-dimensional growth mode is not observed. A considerable number of studies were published regarding the optical properties of the ultrathin CdSe layers in a ZnSe matrix.[3–7,13,15–27] Two interpretations of the spectra regarding the role of the exciton confinement effects were proposed. Some authors argued that the charge carriers and excitons are essentially confined only in one dimension, as expected for a quantum-well system, (e.g., see Refs. 19 and 24–27). The exciton localization within regions of higher Cd concentration is suggested to result in a broad band tail of the excitonic emission. These

localized states were assumed to affect the radiative lifetimes and were regarded as zero-dimensional excitons. Alternatively, other authors (e.g., see Refs. 15, 16 and 20–23) claimed that the optical properties of ultrathin CdSe insertions can be explained only by assuming that all the excitons are laterally confined, and the continuum states do not play a role up to high excitation densities and observation temperatures.

In this study the Cd distribution and morphology of single CdSe layers in a ZnSe matrix were investigated in detail by conventional TEM and HRTEM. Thin layers with $t_n < 3$ ML and a layer with a thickness slightly above the critical one are studied. The distribution of the cadmium is quantitatively derived on an atomic scale from HRTEM images by two different and independent evaluation procedures. The first method is based on the measurement of local lattice parameters by the program DALI (digital analysis of lattice images).[28,29] The second technique CELFA (composition evaluation by lattice fringe analysis)[29–31] relies on the chemical sensitivity of the (002) Bragg reflection.

There are several reasons for the present study. More quantitative data regarding the Cd distribution and the size of the structural features (layer thickness, island sizes) are desirable for the interpretation of the optical spectroscopy data. The study is also motivated by the fact that *ex situ* AFM investigations of bare CdSe islands appear not to be representative of buried structures because the morphology and Cd distribution could be modified during the growth of the ZnSe cap layer.

II. EXPERIMENTAL PROCEDURES

The structures were grown by MBE on GaAs(001) substrates at a temperature of 280 °C. They contain a 50-nm ZnSe-buffer layer and a 10-nm ZnSe cap layer on top of a thin CdSe layer. The intended nominal thicknesses of the CdSe layers are 0.7, 1.25, and 3.6 ML. The details of the growth procedure are outlined by Ivanov *et al.*[24]

The samples were studied by TEM using a Philips CM 200 FEG/ST electron microscope with an electron energy of 200 keV in plan-view and cross-section geometries. The plan-view specimens were prepared by back-side chemical etching using an etching solution consisting of NaOH (1 mol) and 30% H_2O_2 with a proportion of 5:1. The cross-section specimens were thinned by mechanical grinding, dimpling, and subsequent ion etching with Ar^+ or Xe^+ ions at 3 keV with 1 mA.

The composition in the region of the CdSe layer is derived on an atomic scale from HRTEM images. The evaluation procedure DALI requires the measurement of the local lattice parameters, which are determined by the local cadmium concentration x_{Cd} according to Vegard's law

$$a_{\mathrm{Cd}_x\mathrm{Zn}_{1-x}\mathrm{Se}} = a_{\mathrm{ZnSe}} + x_{\mathrm{Cd}}(a_{\mathrm{CdSe}} - a_{\mathrm{ZnSe}}), \tag{1}$$

where $a_{\mathrm{Cd}_x\mathrm{Zn}_{1-x}\mathrm{Se}}$, a_{CdSe}, and a_{ZnSe} are the bulk lattice parameters of the ternary compound and the binary materials.

The HRTEM images are typically taken along the $\langle 110\rangle$-zone axis. After the noise reduction by a Wiener filtering procedure,[28] the positions of the intensity maxima are determined, whose distances can be considered as a fingerprint of the local lattice parameter if the specimen thickness and defocusing distance do not significantly change in the image area of interest. The intensity maxima positions allow the subdivision of the image into unit cells of the size $a_{001} \times a_{110}$ (a_{001} and a_{110} are the distances of the (001) and (110) lattice planes).

The composition in each image unit cell is deduced according to Vegard's law, taking into account the tetragonal distortion of the coherently strained $\mathrm{Cd}_x\mathrm{Zn}_{1-x}\mathrm{Se}$ layer, which increases the lattice parameter along the [001] growth direction $a_{001,\mathrm{Cd}_x\mathrm{Zn}_{1-x}\mathrm{Se}}$. Two limiting cases can be distinguished for the tetragonal distortion in TEM samples. The distortion of a thick sample corresponds to the bulk case. For HRTEM specimens with typical thicknesses of less than 15 nm, an additional elastic relaxation must be considered along the electron-beam direction. According to elasticity theory, the mismatch for a coherently strained structure along the [001] growth direction in the two limiting cases of a thick and a very thin specimen is given by

$$\frac{a_{001,\mathrm{Cd}_x\mathrm{Zn}_{1-x}\mathrm{Se}} - a_{\mathrm{ZnSe}}}{a_{\mathrm{ZnSe}}} = \alpha^{\mathrm{thick,thin}} \frac{a_{\mathrm{Cd}_x\mathrm{Zn}_{1-x}\mathrm{Se}} - a_{\mathrm{ZnSe}}}{a_{\mathrm{ZnSe}}} = \alpha^{\mathrm{thick,thin}} f, \tag{2}$$

with

$$\alpha^{\mathrm{thick}} = \left(1 + 2\frac{C_{12}}{C_{11}}\right) \quad \text{and}$$

$$\alpha^{\mathrm{thin}} = \left(1 + 4\frac{C_{44}C_{12}}{C_{11}^2 + 2C_{11}C_{44} + C_{11}C_{12} - C_{12}^2}\right),$$

where $a_{\mathrm{Cd}_x\mathrm{Zn}_{1-x}\mathrm{Se}}$ denotes the bulk $\mathrm{Cd}_x\mathrm{Zn}_{1-x}\mathrm{Se}$ lattice parameter, C_{ij} the elastic constants of the $\mathrm{Cd}_x\mathrm{Zn}_{1-x}\mathrm{Se}$ layer, and f the lattice-parameter mismatch between the bulk lattice parameters. The Cd concentration x_{Cd} can be deduced from Eqs. (1) and (2):

$$x_{\mathrm{Cd}} = \frac{a_{001,\mathrm{Cd}_x\mathrm{Zn}_{1-x}\mathrm{Se}} - a_{\mathrm{ZnSe}}}{\alpha^{\mathrm{thick,thin}}(a_{\mathrm{CdSe}} - a_{\mathrm{ZnSe}})}. \tag{3}$$

The coefficients of the tetragonal strain for a thin sample ($\alpha^{\mathrm{thin}} = 1.66$) and a thick ($\alpha^{\mathrm{thick}} = 2.3$) sample are almost independent of the Cd concentration. More details of the evaluation procedure were outlined by Rosenauer and co-workers.[28,29]

The alternative method CELFA relies on the chemical sensitivity of the {002} reflections in lattice fringe images, which are obtained by strongly exciting only the (000) and (040) reflections close to the $\langle 100\rangle$-zone axis. The chemically sensitive (020) reflection between the (000) and (040) reflections is centered on the optic axis. The images are taken by transmitting the (000), (020), and (040) reflections through the objective aperture. A defocus series of images with defocus steps of approximately 10 nm is recorded with a CCD camera. After the noise reduction by a Wiener filtering procedure, the lattice fringe images are subdivided into image unit cells of the size of the projected unit cell. Each image unit cell is Fourier transformed. The procedure for the

determination of the local sample thickness and the relevant imaging parameters in regions of known composition, e.g., in the ZnSe, was outlined by Rosenauer and Gerthsen.[29,31] Knowing the specimen thickness and the imaging conditions, the Cd concentration in each image unit cell is obtained by the comparison of the amplitudes of the (000), (020), and (040) beams in the $Cd_xZn_{1-x}Se$, with the respective amplitudes of simulated images for the whole range of Cd concentrations. The image simulations were carried out with the EMS program package,[32] using the Bloch-wave method.

III. EXPERIMENTAL RESULTS

Figure 1 shows plan-view images taken under (**g**/3**g**) weak-beam (WB) conditions with $\mathbf{g}=(220)$ for different nominal CdSe thicknesses: 0.7 ML (a), 1.25 ML (b), and 3.6 ML (c). The fine speckle contrast is interpreted in terms of small islands with a size of less than 10 nm. The change of the thickness and bending of the TEM specimen induces the coarse bright and dark bands. The island density increases with the nominal CdSe thickness from 3×10^{11} cm^{-2} for 0.7 ML (a) to 5×10^{11} cm^{-2} for 1.25 ML (b) and 7×10^{11} cm^{-2} for 3.6 ML (c). It is worth noting that the small islands can only be seen under (220) WB conditions. They are almost invisible under different imaging conditions, e.g., bright-field or WB imaging with $\mathbf{g}=(2\bar{2}0)$. This effect is probably due to a shape asymmetry of the small islands, which will be further discussed in Sec. IV. In addition, larger islands with a lateral extension up to 40 nm and with a density of 5×10^{9} cm^{-2} can be observed in Fig. 1(c) for $t_n=3.6$ ML. The $Cd_xZn_{1-x}Se$ islands are completely strained because misfit dislocations were not observed.

Figure 2 shows images of a big island in the 3.6-ML specimen under different imaging conditions. The plan-view bright-field image [Fig. 2(a)] was taken in a [001] zone-axis orientation. Figures 2(a) and 2(c) are (**g**/3**g**) WB images with $\mathbf{g}=(2\bar{2}0)$ and $\mathbf{g}=(220)$. Although the strain contrast does not allow an exact size determination, the oval shape of the island can be recognized. The HRTEM cross-section image [Fig. 2(d)] was taken along the $[1\bar{1}0]$-zone axis, where an island is visible along its large extension. An estimation of the island sizes yields 15 ± 2 and 35 ± 5 nm along the two $\langle110\rangle$ directions.

Figure 3 shows a noise-filtered HRTEM image along the $[1\bar{1}0]$ zone axis (a), and the results obtained by the DALI evaluation [(b) and (c)] for the specimen with $t_n=1.25$ ML. The local lattice parameters are displayed in Fig. 3(b) in a color-coded map in units of $a_{001,Cd_xZn_{1-x}Se}/a_{ZnSe}$. The measured layer thickness between 5 and 9 ML distinctly deviates from the nominal thickness of 1.25 ML. A laterally inhomogeneous Cd concentration is evident from the variations of the local lattice parameter. The lattice-parameter misfit along the [001] direction reaches about 8% in the island in the center, yielding a maximum cadmium concentration $x_{Cd}=55\pm8\%$ Cd according to Eq. (3). The error is mainly determined by the uncertainty in the specimen thickness, which is responsible for the elastic relaxation along the electron-beam direction. The small regions in the ZnSe matrix in the Fig. 3(b), where Cd appears to be present, are most likely induced by residual noise or a local change of the imaging conditions, e.g., a local crystal tilt or thickness fluctuations of the specimen.

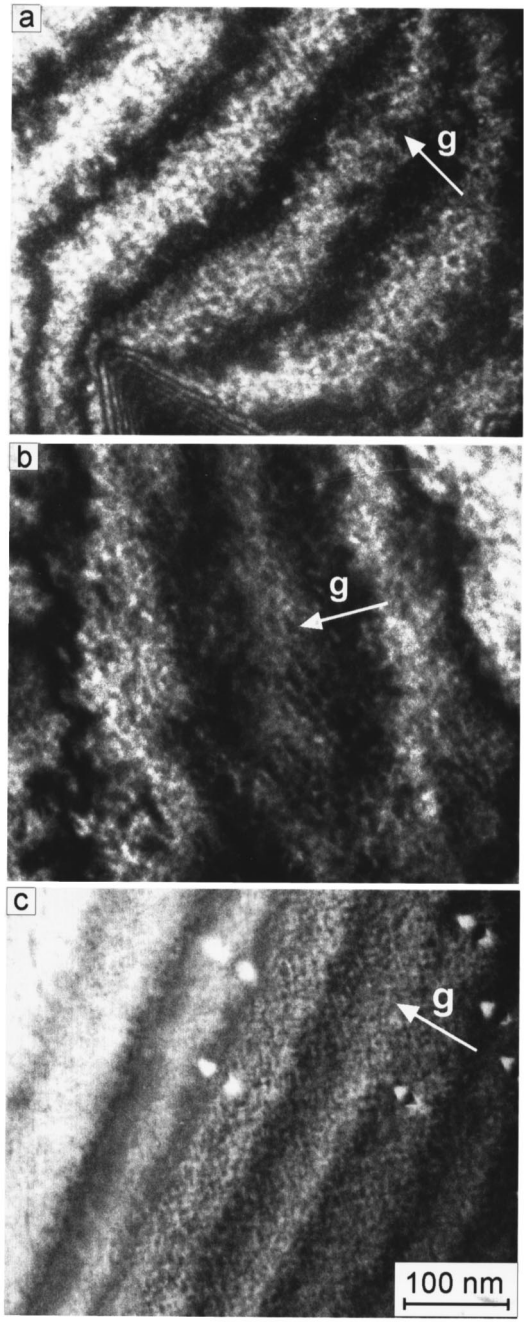

FIG. 1. Dark-field plan-view images of the ZnSe/CdSe/ZnSe heterostructures under (**g**/3**g**) weak-beam conditions with $\mathbf{g}=(220)$ for different nominal CdSe thicknesses: 0.7 ML (a), 1.25 ML (b), and 3.6 ML (c).

Another effect of the lattice-parameter increase by the Cd is a displacement U of the lattice positions in the $Cd_xZn_{1-x}Se$ layer with respect to a reference lattice extrapolated from the ZnSe over the Cd-rich region. The local displacements of each image unit cell with respect to the ZnSe reference lattice along the growth direction are shown in Fig. 3(c). The red color, indicating large displacements on top of the island marked by *A*, visualizes the upward bending of the lattice planes which is associated with the high Cd content. The total amount of the cadmium contained in the layer

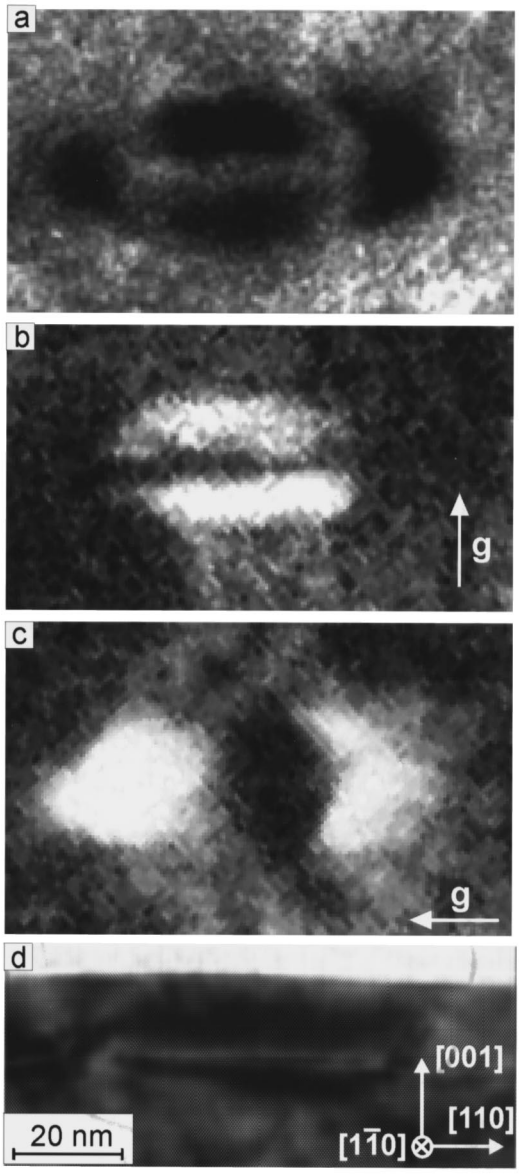

FIG. 2. Plan-view images of a big island at a nominal CdSe layer thickness of 3.6 ML. (a) Bright-field image along the [001]-zone axis. (b) (**g**/3**g**) weak-beam conditions with $\mathbf{g}=(2\bar{2}0)$. (c) (**g**/3**g**) weak-beam conditions with $\mathbf{g}=(220)$. (d) Cross-section $[1\bar{1}0]$-HRTEM image.

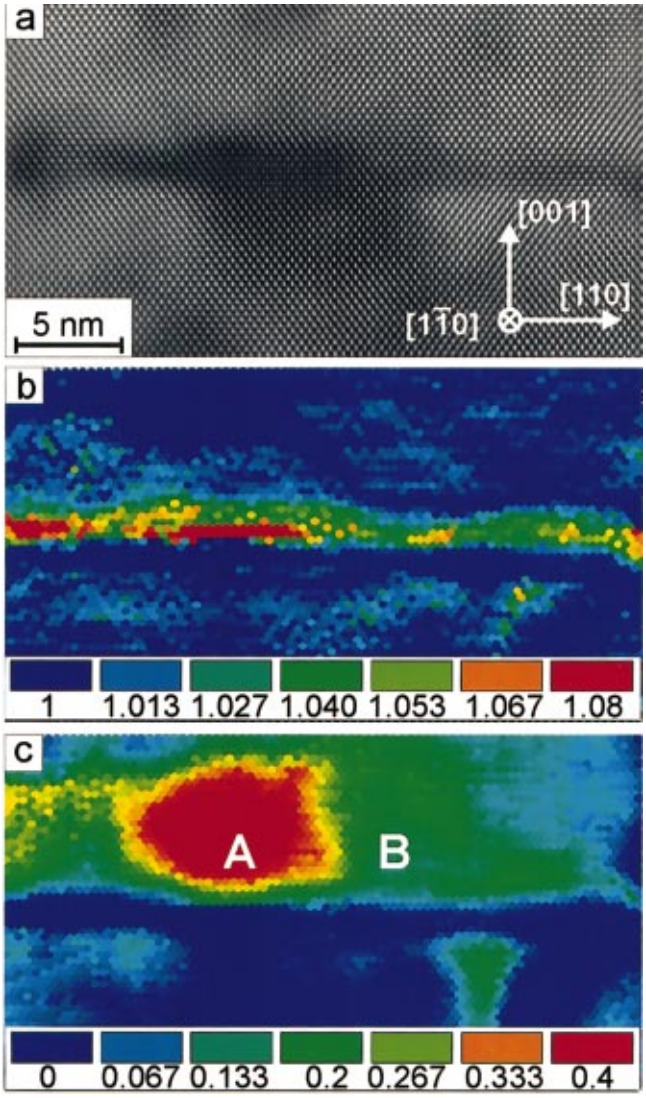

FIG. 3. (Color) (a) $[1\bar{1}0]$-HRTEM image of the CdSe layer with a nominal thickness of 1.25 ML. (b) Color-coded maps of the local lattice parameters in units of $a_{001,\mathrm{Cd}_x\mathrm{Zn}_{1-x}\mathrm{Se}}/a_{\mathrm{ZnSe}}$. (c) Component of the local displacements along the $[00\bar{1}]$ direction.

C_{CdSe} in units of CdSe ML is given by

$$C_{\mathrm{CdSe}}=\frac{U_{\max}}{\alpha^{\mathrm{thick,thin}} f_0}, \tag{4}$$

where $U_{\max}$ is the maximum displacement on top of the $\mathrm{Cd}_x\mathrm{Zn}_{1-x}\mathrm{Se}$ layer, and f_0 the misfit between the bulk lattice parameters of the binary compounds. The value $U_{\max}=0.4$ for the Cd-rich inclusion (region A) corresponds to $C_{\mathrm{CdSe}}=2.9\pm0.5$ ML. The error is determined by the thin/thick foil approximation given by Eq. (4). Region B, with the lower Cd concentration next to the island, contains only 1.3 ± 0.2 ML CdSe.

Figure 4 shows a lattice fringe image with a superimposed color-coded map of the local Cd content for the specimen

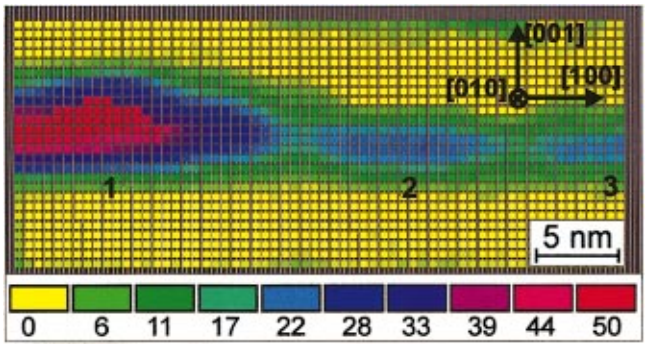

FIG. 4. (Color) Color-coded map of the local Cd content obtained by CELFA for the CdSe layer with $t_n=3.6$ ML superimposed on a lattice fringe image. Region 1 marks a part of a large island. Regions 2 and 3 denote small islands.

TABLE I. Measured Cd concentration in the islands by the methods DALI and CELFA.

Nominal CdSe thickness (ML)	Cd concentration [%] DALI	Cd concentration [%] CELFA
0.7	12–25	10–16
1.25	25–55	20–30
3.6	30–60 (small islands) 70 (large islands)	22–32 (small islands) 50 (large islands)

with $t_n = 3.6$ ML obtained by CELFA. The faint bright lines which are visible at the borders of the color-coded map represent the (002) planes. The yellow regions correspond to the ZnSe and the green to red regions show the Cd content in the $Cd_xZn_{1-x}Se$ layer. Again, a significant broadening of the $Cd_xZn_{1-x}Se$ compared to the nominal layer thickness is observed. Three regions with an elevated Cd content can be distinguished. Region 1 is part of a large island, where the Cd concentration reaches 50%. Regions 2 and 3 are small islands, with an extension smaller than 10 nm and a Cd concentrations up to 23% which are separated by narrow regions with only 17% Cd.

Table I summarizes the measured Cd concentrations for islands in the different samples. A distinction was made between small and large islands for $t_n = 3.6$ ML and between the results of the two techniques. The CELFA measurements typically yield lower Cd concentrations compared to the DALI results, which are average concentrations derived from the thin/thick specimen approximation. The discrepancy between the DALI and CELFA results can be partially explained by the higher inaccuracy of the DALI evaluations. The error for the measured lattice plane distances is larger in regions with large gradients of the specimen thickness or composition. In addition, there is a tendency to discard DALI evaluations with low Cd concentrations which are typically affected by noise despite the applied noise reduction procedures. The true Cd concentration of the islands must be assumed to be higher than the measured value due to the composition averaging along the specimen thickness, which will be shown in Sec. IV of this paper.

Figure 5 shows Cd-concentration profiles obtained by CELFA along the [001] growth direction for all investigated specimens. These evaluations were carried out in regions between the Cd-rich islands, e.g., for the sample with $t_n = 3.6$ ML CdSe between islands 2 and 3 in Fig. 4. The Cd content was averaged along the horizontal [100] direction. The calculated full widths at half maximum of the Cd profiles are 7.5 ML for $t_n = 0.7$ ML, 8.5 ML for $t_n = 1.25$ ML, and 11 ML for $t_n = 3.6$ ML. The total CdSe content obtained by the integration of the curves increases with t_n and corresponds to 0.3, 0.7, and 1.7 ML, which amounts to approximately 50% of the nominal CdSe content.

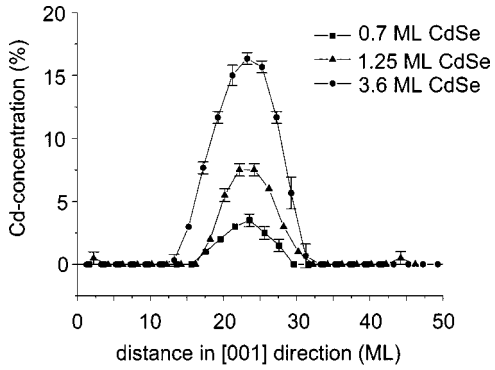

FIG. 5. Cd concentration profiles from regions with a low Cd concentration between the islands for the different nominal CdSe thicknesses.

IV. DISCUSSION

A. Cd distribution and growth mechanisms

The TEM characterization and the composition evaluation yield a detailed picture of the morphology and Cd distribution of ultrathin CdSe layers in a ZnSe matrix. Instead of binary CdSe layers, the results of the composition analyses reveal a two-dimensional ternary $Cd_xZn_{1-x}Se$ layer with a fairly homogeneous thickness, which contains Cd-rich inclusions. The Cd-concentration profiles of the 2D layers (Fig. 5) show, that the real layer thickness does not increase proportionally to t_n, in contrast to the maximum Cd concentration which significantly rises from 3% to 7.5% and 16%.

The layer morphology for $t_n = 0.7$ and 1.25 ML does not comply with the typical SK structure, where islands on a thin wetting layer are expected. A morphology better compatible with the SK mode can be assigned to the specimen with $t_n = 3.6$ ML, where large islands are additionally observed whose heights exceed the 2D $Cd_xZn_{1-x}Se$ layer thickness (Fig. 4). The transition from the two-dimensional to the three-dimensional growth mode at $t_n \geqslant 3$ ML is in agreement with the literature.[3,4,17] However, the small islands are already present prior to the 2D/3D transition.

A correlation between the small-scale speckle contrast in the plan-view images and the Cd-rich inclusions in the $Cd_xZn_{1-x}Se$ appears reasonable because the sizes and distances agree in the plan-view and cross-section images. The difference is that the chemical analyses allow a more precise evaluation of the sizes of the Cd-rich inclusions than the strain contrast of the plan-view images. Small islands with extensions between 3 and 7 nm and a density of 3×10^{11} cm^{-2} are already detected in the sample with $t_n = 0.7$ ML. The sizes of the small islands do not significantly depend on t_n, while the island density approaches 7×10^{11} cm^{-2} at 3.6-ML CdSe. However, the main effect of the increase of the nominal CdSe content is the enlargement of the Cd concentration in the small islands from 10% to 60% according to Table I.

It can be stated as a summary of the quantitative composition analyses that the variation of t_n between 0.7 and 3.6 ML only slightly affects the real layer thickness and the island sizes. The increasing amount of deposited CdSe is mainly accommodated by a rising Cd concentration in the 2D $Cd_xZn_{1-x}Se$ layer and in the small islands.

The Cd-concentration profiles (Fig. 5) also contain some information about the origin of broadening of the CdSe layers. Since the profiles exhibit an almost symmetrical shape, interdiffusion is the most likely cause. Segregation could also induce the spreading of the Cd distribution. However, asymmetrical profiles would be expected, if segregation was

the dominant mechanism. In addition, a segregation model introduced by Muraki *et al.*[33] did not allow a decent fit of the experimental data. The diffusion distance L_D of Cd in ZnSe is obtained by fitting the solution of Fick's law with the appropriate starting and boundary conditions[34] to the experimental profiles. L_D increases with the nominal CdSe thickness from 4.5 to 5.6 ML. However, the increase is not considered to be significant due to the error introduced by the specimen tilt that is required for the CELFA technique. A diffusion coefficient D can be calculated on the basis of the measured L_D according to $L_d=2\sqrt{Dt}$, where the diffusion time $t\approx 100$ sec corresponds to the duration of the cap layer growth. A high diffusion coefficient $D\sim 5\times 10^{-15}$ $\mathrm{cm}^2\,\mathrm{sec}^{-1}$ is deduced from the averaged diffusion lengths which is at the upper limit of the range of diffusion coefficients measured by Kuttler *et al.*[35] Similarly, high diffusion coefficients were obtained for samples with CdSe layers grown by migration enhanced epitaxy, where a detailed evaluation of the broadening of the CdSe layer was performed taking into account the influence of the CdZn interdiffusion, the cadmium segregation and the sample tilt.[36]

An asymmetry of the island extensions was directly observed for the large three-dimensional islands (Fig. 2). An indication for an asymmetry of the small islands is obtained by the fact that the islands can only be imaged under weak-beam conditions with $\mathbf{g}=(220)$ while they are invisible with a $\mathbf{g}=(2\bar{2}0)$ imaging vector. However, a more detailed specification of the type of asymmetry (size and/or shape) is not possible for the small islands. Further evidence for a possible asymmetry of the small islands is obtained by photoluminescence spectroscopy measurements of CdSe/ZnSe superlattices along the $[110]$ and $[1\bar{1}0]$ directions[37] which were grown under similar conditions. Only speculations are possible about the origin of the asymmetry. A shape asymmetry of two-dimensional InAs islands on vicinal GaAs(001) surfaces was found by Bressler-Hill *et al.*[38] for a coverage of 0.75 ML by scanning tunneling microscopy. Here, the InAs islands increases their sizes in one of the $\langle 110\rangle$ directions on a (2×4)-reconstructed GaAs(001) surface independent of the substrate misorientation which the authors explained by the effect of strain relaxation during the island growth as also suggested by Tersoff and Trump.[39] Another possible origin could be related to different surface diffusion coefficients along the $[110]$ and $[1\bar{1}0]$ directions, which were calculated in Ref. 40 for Ga and Al on the (2×4)-reconstructed GaAs(001) surface. Although data about the Cd diffusion coefficient on ZnSe(001) are not available, a similar effect is conceivable for ZnSe(001) with surface reconstructions exhibiting dimers, e.g., the (2×1) reconstruction under Se-rich growth conditions.

B. Influence of the averaging along the TEM sample thickness on the measured Cd concentrations

The following considerations are presented to assess the influence of the averaging along the electron-beam direction and to obtain an estimate of the true maximum Cd concentration in the Cd-rich inclusions. The probability for an island to be completely contained in a TEM cross-section specimen increases with decreasing island size and increasing island density. The distances between the centers of small islands of 12 to 18 nm can be calculated according to $1/\sqrt{N_{\mathrm{dot}}}$ (N_{dot} is the density of the small islands) which are comparable to typical measured specimen thicknesses for the CELFA procedure of 15 ± 2 nm. With small island extensions below 10 nm, a significant fraction of the islands should be completely trapped in the TEM sample. The situation for the cross-section imaging is schematically shown in Fig. 6. The Cd concentration in the islands will be reduced at a specimen thickness of 15 nm due to the averaging, even if the island is completely trapped in the TEM sample. Alternatively, the cross-section specimens may only contain a part of an island. Steps at the ZnSe/CdSe interface may lead to a local broadening of the $Cd_xZn_{1-x}Se$ layer.

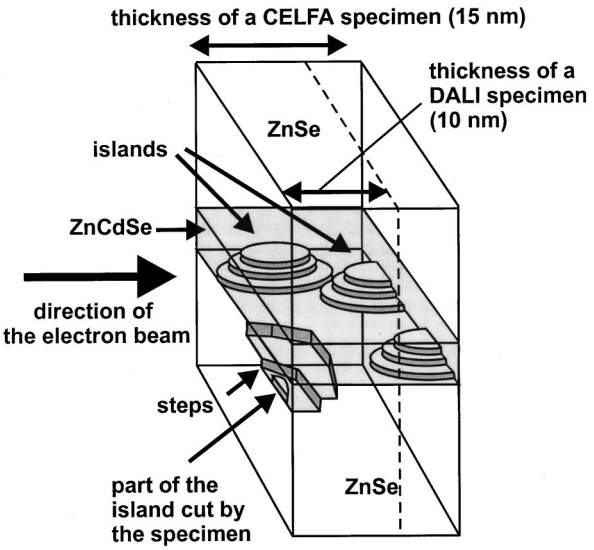

FIG. 6. Schematic illustration of a TEM cross-section sample containing Cd-rich islands embedded in a $Cd_xZn_{1-x}Se$ layer with a lower Cd concentration.

The specimen thickness of 15 nm represents a worst case as far as the averaging is concerned because the regions for the DALI evaluations are generally thinner. Accurate measurements of the HRTEM specimen thicknesses yielding typical values between 2 and 10 nm could be performed for the $In_xGa_{1-x}As$ system[29,41] which can be considered to be comparable to the $Cd_xZn_{1-x}Se$ system. Another origin of the systematically higher Cd concentrations in islands obtained by the DALI evaluations—apart from the reasons already mentioned in Sec. III—can therefore be that the averaging in the thinner DALI specimens does not necessarily include the surrounding $Cd_xZn_{1-x}Se$ layer.

Alternatively, the situation has to be considered where Cd-rich islands are surrounded by pure ZnSe. It is conceivable that a continuous layer could be visible in cross-section images at small island distances, high island densities and the sample thicknesses for the CELFA procedure. However, isolated islands should have been occasionally visible in the thin sample regions for the DALI evaluations which never occurred. Therefore, the presence of a continuous $Cd_xZn_{1-x}Se$ layer is indeed highly probable.

An idea of the true Cd concentration in an island corresponding to that marked by ''2'' in Fig. 4 is obtained by the following procedure. A measured Cd-concentration profile along the horizontal [100] direction is plotted in Fig. 7(a). We assume for the modeling of the Cd distribution that the

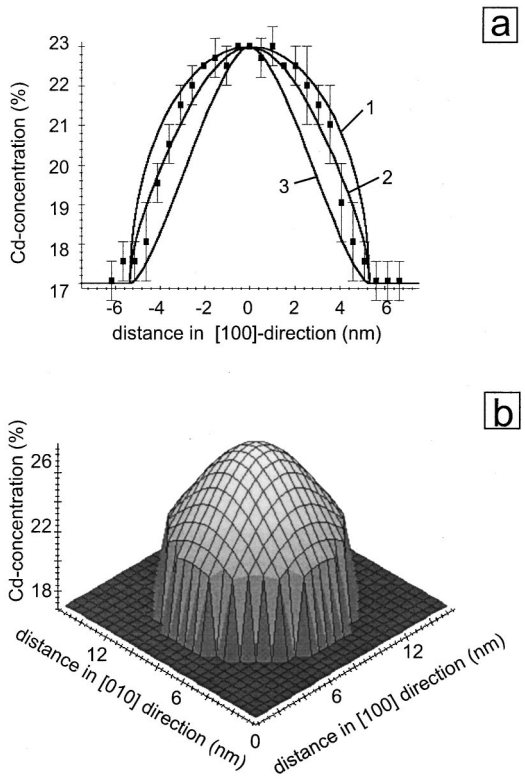

FIG. 7. Modeling of the true Cd concentration in island 2 of Fig. 4 for a sample thickness of 15 nm along the [010] direction. (a) Experimental Cd profile along the [100] direction, and calculated composition profiles based on different functions for the Cd distribution: (1) constant, (2) Gauss, and (3) linear. (b) Three-dimensional visualization of the Gaussian-shaped Cd distribution.

island is entirely enclosed and centered in the TEM specimen as well as a radial symmetry of the lateral Cd distribution. Three models with different concentration profiles were tested to fit the experimental Cd profile: (1) a constant, (2) a Gaussian-shaped, and (3) a linear profile. As an example, the Gaussian-shaped Cd distribution is displayed three dimensionally in Fig. 7(b). An integration along the [010] electron-beam direction is performed to obtain the averaged Cd content which is compared with the experimental data. The results for the different model profiles are also included in Fig. 7(a). Obviously, the best agreement is obtained for model (2) shown in Fig. 7(b), where the maximum Cd concentration at the center is 28% in contrast to the measured Cd concentration of only 23%. It is therefore concluded that the small islands do not consist of pure CdSe but contain only slightly higher Cd concentrations compared to the measured values. In contrast to the small islands, a core of pure CdSe appears to be possible for the large islands in the 3.6-ML sample, which exhibit the highest measured Cd concentrations. Due to the large distances between the islands, there is a low probability that an island is completely contained in the cross-section sample which artificially reduced the measured Cd concentration.

V. SUMMARY

Two-dimensional ternary $Cd_xZn_{1-x}Se$ layers are observed when CdSe with a nominal thickness between 0.7 and 3.6 ML is inserted in a ZnSe matrix by MBE. The layers contain regions with an enlarged Cd concentration and lateral extensions below 10 nm which are considered as small islands. We have demonstrated that the real layer thickness and the sizes of the small islands do not significantly increase with t_n. Instead, the additional CdSe is accommodated by the rise of the Cd concentration from 3% to 16% in the 2D layer, and from approximately 10% to 60% in the small islands. The symmetrical concentration profiles along the growth direction indicate that interdiffusion is the dominant broadening mechanism as opposed to cadmium segregation where an asymmetric profile is expected. It was demonstrated by the modeling of the averaging effect along the TEM specimen thickness that the small islands cannot consist of pure CdSe. The results of our analyses profile a basis for the modeling of the confinement potential which will significantly contribute to the proper interpretation of the optical spectroscopy data.

Larger islands with a lower density are found at $t_n = 3.6$ ML, which is compatible with the Stranski-Krastanow transition from the two- to three-dimensional growth mode typically occurring at 3 ML. Higher Cd concentrations are measured in these islands, which possibly contain a core of pure CdSe. Asymmetrical dimensions along the two different $\langle 110 \rangle$ directions were measured for the large islands. The imaging behavior of the small islands also indicates an asymmetry. The asymmetry could be related to the anisotropic surface reconstruction, which may cause an orientation-dependent relaxation behavior of the islands or direction-dependent surface diffusion coefficients.

ACKNOWLEDGMENTS

The authors are very much indebted to Dr. S. V. Ivanov (A. F. Ioffe Physical-Technical Institute of the Russian Academy of Sciences, St. Petersburg) for providing the samples, and for fruitful discussions. The support of the Deutsche Forschungsgemeinschaft (DFG) under Contract No. Ge 841/7-1 is gratefully acknowledged.

[1] A. Madhukar, Thin Solid Films **231**, 8 (1993).
[2] D. Bimberg, M. Grundmann, and N. N. Ledentsov, *Quantum Dot Heterostructures* (Wiley, New York, 1998).
[3] S. Fujita, Y. Wu, Y. Kawakami, and S. Fujita, J. Appl. Phys. **72**, 5233 (1992).
[4] M. Rabe, M. Lowisch, and F. Henneberger, J. Cryst. Growth **184/185**, 248 (1998).
[5] S. H. Xin, P. D. Wang, Aie Yin, C. Kim, M. Dobrovolska, J. L. Merz, and J. K. Furdyna, Appl. Phys. Lett. **69**, 3884 (1996).
[6] D. Hommel, K. Leonardi, H. Heinke, H. Selke, K. Ohkawa, F. Gindele, and U. Woggon, Phys. Status Solidi B **202**, 835 (1997).
[7] I. Suemune, K. Uesugi, H. Suzuki, H. Nashiki, and M. Arita, Phys. Status Solidi B **202**, 845 (1997).
[8] M. Arita, A. Avramescu, K. Uesugi, I. Suemune, T. Numai, H.

Machida, and N. Shimoyama, Jpn. J. Appl. Phys. **36**, 4097 (1997).
[9] J. L. Merz, S. Lee, and J. K. Furdyna, J. Cryst. Growth **184/185**, 228 (1998).
[10] M. Grün, F. Funfrock, P. Schunk, Th. Schimmel. M. Hetterich, and C. Klingshirn, Appl. Phys. Lett. **73**, 1343 (1998).
[11] T. Shubina, S. Sorokin, A. Toropov, I. Sedova, A. Sitnikova, A. V. Ankudinov, A. N. Titkov, S. Ivanov, I. Yamakawa, M. Ichida, and A. Nakamura, 24th International Conf. on Phys. Semicon., p. 77 (World Scientific, Singapore, 1999).
[12] J. B. Smathers, E. Kneedler, B. R. Bennett, and B. T. Jonker, Appl. Phys. Lett. **72**, 1238 (1998).
[13] K. Leonardi, H. Selke, H. Heinke, K. Ohkawa, D. Hommel, F. Gindele, and U. Woggon, J. Cryst. Growth **184/185**, 259 (1998).
[14] H. Kirmse, R. Schneider, M. Rabe, W. Neumann, and F. Henneberger, Appl. Phys. Lett. **72**, 1329 (1998).
[15] M. Strassburg, V. Kutzer, U. W. Pohl, A. Hoffmann, I. Broser, N. N. Ledentsov, D. Bimberg, A. Rosenauer, U. Fischer, D. Gerthsen, I. L. Krestnikov, M. V. Maximov, P. S. Kop'ev', and Zh. I. Alferov, Appl. Phys. Lett. **72**, 942 (1998).
[16] T. Kümmell, R. Weigand, G. Bacher, A. Forchel, K. Leonardi, D. Hommel, and H. Selke, Appl. Phys. Lett. **73**, 3105 (1998).
[17] K. P. O'Donnell, K. Chinyama, P. J. Parbrook, A. Rosenauer, M. Umlauff, H. Kalt, and D. Gerthsen, J. Cryst. Growth **184/185**, 1331 (1998).
[18] K. Chinyama, K. P. O'Donnell, A. Rosenauer, and D. Gerthsen, J. Cryst. Growth **203**, 362 (1999).
[19] U. Neukirch, D. Weckendrup, W. Fashinger, P. Juza, and H. Sitter, J. Cryst. Growth **138**, 849 (1994).
[20] F. Flack, N. Samarth, V. Nikitin, P. A. Crowell, J. Shi, J. Levy, and D. D. Awschalom, Phys. Rev. B **54**, R17 312 (1996).
[21] N. N. Ledentsov, I. L. Krestnikov, M. V. Maximov, S. V. Ivanov, S. L. Sorokin, P. S. Kop'ev, Zh. I. Alferov, D. Bimberg, and C. M. Sotomayor Torres, Appl. Phys. Lett. **69**, 1343 (1996); **70**, 2766 (1997).
[22] I. L. Krestnikov, M. V. Maximov, A. V. Sakharov, P. S. Kop'ev, Zh. I. Alferov, N. N. Ledentsov, D. Bimberg, and C. M. Sotomayor Torres, J. Cryst. Growth **184/185**, 545 (1998).
[23] U. W. Pohl, R. Engelhardt, V. Türck, and D. Bimberg, J. Cryst. Growth **195**, 569 (1998).
[24] S. V. Ivanov, A. A. Toporov, T. V. Shubina, S. V. Sorokin, A. V. Lebedev, I. V. Sedova, P. S. Kop'ev, G. R. Pozina, J. P. Bergman, and B. Monemar, J. Appl. Phys. **83**, 3168 (1998).
[25] A. A . Toropov, S. V. Ivanov, T. V. Shubina, A. V. Lebedev, S. V. Sorokin, P. S. Kop'ev, G. R. Pozina, J. P. Bergman, and B. Monemar, J. Cryst. Growth **184/185**, 293 (1998).
[26] A. A. Toropov, S. V. Ivanov, T. V. Shubina, S. V. Sorokin, A. V. Lebedev, A. A. Sitnikova, P. S. Kop'ev, M. Willander, G. R. Pozina, J. P. Bergman, and B. Monemar, Jpn. J. Appl. Phys. **38**, 566 (1999).
[27] A. A. Toropov, T. V. Shubina, S. V. Sorokin, A. V. Lebedev, R. N. Kyutt, S. V. Ivanov, M. Karlsteen, M. Willander, G. R. Pozina, J. P. Bergman, and B. Monemar, Phys. Rev. B **59**, R2510 (1999).
[28] A. Rosenauer, S. Kaiser, T. Reisinger, J. Zweck, W. Gebhardt, and D. Gerthsen, Optik (Stuttgart) **102**, 63 (1996).
[29] A. Rosenauer and D. Gerthsen, Adv. Imaging Elecron Phys. **107**, 121-230 (1999).
[30] A. Rosenauer, U. Fischer, D. Gerthsen, and A. Förster, Ultramicroscopy **72**, 121 (1998).
[31] A. Rosenauer and D. Gerthsen, Ultramicroscopy **76**, 49 (1999).
[32] P. A. Stadelmann, Ultramicroscopy **51**, 313 (1987).
[33] K. Muraki, S. Fukatsu, Y. Shiraki, and R. Ito, Appl. Phys. Lett. **61**, 557 (1992).
[34] P. Haasen, *Physical Metallurgy* (Cambridge University Press, Cambridge, 1996), Chap. 8.
[35] M. Kuttler, M. Strassburg, V. Türck, R. Heitz, U. W. Pohl, D. Bimberg, E. Kurz, G. Landwehr, and D. Hommel, Appl. Phys. Lett. **69**, 2647 (1996).
[36] N. Peranio, A. Rosenauer, D. Gerthsen, S. V. Sorokin, I. V. Sedova, and S. V. Ivanov, Phys. Rev. B (to be published).
[37] I. Krestnikov, M. V. Maximov, S. V. Ivanov, S. V. Sorokin, S. A. Permogorov, A. N. Reznitsky, A. V. Kornievsky, P. S. Kop'ev, Zh. I. Alferov, N. N. Ledentsov, D. Bimberg, and C. M. Sotomayor Torres, in *Proceedings of the 23rd International Conference on the Physics of Semiconductors, Berlin, Germany, July 21–26, 1996*, edited by M. Scheffler and R. Zimmermann (World Scientific, Singapore, 1996), Vol. 1, p. 3187.
[38] V. Bressler-Hill, A. Lorke, S. Varma, P. M. Petroff, K. Pond, and W. H. Weinberg, Phys. Rev. B **50**, 8479 (1994).
[39] J. Tersoff and R. M. Trump, Phys. Rev. Lett. **70**, 2782 (1993).
[40] A. Kley, P. Ruggerone, and M. Scheffler, Phys. Rev. Lett. **79**, 5278 (1997).
[41] U. Woggon, W. Langbein, J. M. Hvam, A. Rosenauer, T. Remmele, and D. Gerthsen, Appl. Phys. Lett. **71**, 377 (1997).